PHYSICAL REVIEW B **68**, 214429 (2003)

Temperature evolution of crystal field interactions across the Jahn-Teller transition in a $La_{7/8}Sr_{1/8}MnO_3$ single crystal

G. Alejandro
Centro Atómico Bariloche, Avenida Bustillo 9500, (8400) San Carlos de Bariloche, Río Negro, Argentina

M. C. G. Passeggi
Instituto de Desarrollo Tecnológico, Consejo Nacional de Investigaciones Científicas y Técnicas and Facultad de Bioquímica y Ciencias Biológicas, Universidad Nacional del Litoral, Santa Fe, Argentina

D. Vega
Centro Atómico Constituyentes, CNEA, (1650) San Martín, Pcia de Buenos Aires, Argentina

C. A. Ramos, M. T. Causa, and M. Tovar
Centro Atómico Bariloche, Avenida Bustillo 9500, (8400) San Carlos de Bariloche, Río Negro, Argentina

R. Senis
Institut de Ciencia de Materials de Barcelona, CSIC, Campus UAB, Bellaterra 08193, Catalunya, Spain

(Received 18 December 2002; revised manuscript received 30 June 2003; published 29 December 2003)

We present electron-spin-resonance (ESR), x-ray-diffraction, and dilatometry studies in a $La_{7/8}Sr_{1/8}MnO_3$ single crystal. ESR experiments were performed in the paramagnetic regime ($T_C \approx 180$ K), from 220 K to 570 K at a microwave frequency of 9.4 GHz. We measured the ESR linewidth as a function of temperature with the static magnetic field **H** parallel to the crystallographic directions [100] and [001], referred to as the orthorhombic (*Pbnm*) axes. Detailed angular variations at constant temperature for **H** rotating in the (001), (010) and $(\overline{1}10)$ planes were also performed. The temperature dependence of the linewidth for fixed directions clearly reflects the changes in the symmetry of the crystal. At the Jahn-Teller (JT) transition, a very noticeable decrease of the linewidth is observed. The angular dependence of the linewidth reveals an anisotropy that is temperature dependent. The amplitude of the variations decreases with T and almost disappears above $T_{JT} \approx 280$ K. However, there is a small remnant anisotropy present up to 400 K. We have carefully investigated the temperature dependence of this anisotropy across the Jahn-Teller transition. We showed that it is related with the evolution of the crystal field interactions. The symmetry of the ESR spectra is explained in terms of a spin Hamiltonian that includes isotropic Heisenberg superexchange, single-ion-crystal field, and Dzyaloshinsky-Moriya antisymmetric exchange. The experimental angular variation of the ESR linewidth and its temperature dependence were fitted using the calculated expression for the linewidth as obtained from a perturbative Kubo-Tomita approach. From the ESR data we have obtained a ratio $\widetilde{E}/\widetilde{D} = -0.4(1)$ for the spin Hamiltonian coefficients associated with the orthorhombic ($\widetilde{E}$) and tetragonal ($\widetilde{D}$) Jahn-Teller distortions of the MnO_6 octahedra. The temperature dependence of the parameters of the model is presented and the correlation with the dilatometry results are discussed.

DOI: 10.1103/PhysRevB.68.214429 PACS number(s): 76.30.−v, 75.10.Dg, 75.47.Lx, 75.47.Gk

I. INTRODUCTION

In recent years, there have been renewed efforts in the study of mixed-valence manganites. This is due to the colossal magnetoresistance (CMR) and the interesting correlation between structural, magnetic, and transport properties that they exhibit.

In $LaMnO_3$, parent compound of the hole doped CMR $La_{2/3}Sr_{1/3}MnO_3$, all the Mn ions are Mn^{3+} ($t_{2g}^3 e_g^1$). The crystalline structure (orthorhombic O' phase) is strongly distorted due to a cooperative Jahn-Teller (JT) effect, below[1] $T_{JT} \approx 700$ K. Above T_{JT} the structure evolves to a much less distorted, also $Pbnm$ orthorhombic, O phase. The structural deformations consist of JT distortions and tilting of the MnO_6 octahedra. Below T_{JT} three different Mn-O distances have been determined.[2] When increasing the temperature towards T_{JT}, these differences diminish and the three distances become almost equal in the O phase. At $T_R = 1010$ K a second structural transition to a rhombohedral ($R\overline{3}c$) R phase takes place. The tilting of the octahedra results in Mn-O-Mn angles smaller than 180°, typically between 155° and 158° in the orthorhombic phases and ≈160° in the rhombohedral phase.[2]

In $La_{1-x}Sr_xMnO_3$ it has been observed that the magnitude of the lattice distortion decreases with the Sr content[3] and so does the JT transition temperature[4,5] down to ≈220 K for $x \approx 0.15$. These lightly hole doped samples are intermediate between an antiferromagnetic insulator for $x=0$ and a metallic ferromagnet (FM) for $x \gtrsim 0.15$. In the case of $x=1/8$ four characteristic temperatures have been associated with structural and magnetic transitions. A FM state is found below $T_C = 180$ K, metallic down to 150 K and insulating below this temperature. This change is accompanied by a struc-

©2003 The American Physical Society

tural transition to a new orthorhombic phase O''. Around $T_{JT} = 280$ K, the Jahn-Teller transition occurs[6] from the O' to the O phase. Above $T_R = 475$ K, the R phase is observed.[6]

It has been shown[7] for polycrystalline $\mathrm{LaMnO}_{3+\delta}$ that the electron-spin-resonance (ESR) linewidth is directly correlated with the magnitude of the JT distortions through the anisotropic crystal field. The Dzyaloshinsky-Moriya (DM) antisymmetric superexchange interactions, associated with the tilting of the octahedra, also add to the line broadening. Both contributions are exchange narrowed by Heisenberg isotropic interactions. Thus, this experimental technique is a useful tool for studying the T evolution of the lattice distortions.

ESR has also been applied[4,8,9] to the study of the JT effect in $\mathrm{La}_{1-x}\mathrm{Sr}_x\mathrm{MnO}_3$ with $x \leq 0.20$. These studies, in single-crystal materials, revealed a temperature-dependent anisotropic ESR linewidth with characteristic features around T_{JT}. Detailed angular dependence at fixed temperatures has been reported[8,10] for $x = 1/8$ and $x = 0.05$.

The Sr concentration $x = 1/8$ is particularly interesting because it allows the study of the different structural phases at accessible temperatures. In this work, we report x-ray-diffraction, thermal-expansion, dc-susceptibility, and ESR measurements carried on a $\mathrm{La}_{7/8}\mathrm{Sr}_{1/8}\mathrm{MnO}_3$ single crystal in a broad temperature range. We analyzed the twin structure of this particular crystal and correlate the dc-susceptibility, dilatometry, and ESR results drawing a complete picture of the temperature evolution of the cooperative JT effect. We explain the ESR linewidth and resonance field anisotropy and its variation with temperature in terms of a Kubo-Tomita perturbational formalism.

II. EXPERIMENTAL

A. Sample preparation and experimental techniques

A $2.6 \times 1.6 \times 1.1\ \mathrm{mm}^3$ single crystal of $\mathrm{La}_{7/8}\mathrm{Sr}_{1/8}\mathrm{MnO}_3$ was grown by the floating-zone method[11] and it was oriented at room temperature employing the precession camera x-ray diffraction method. Thermal expansion was measured along different axes using a three terminal capacitance method[12] from 80 to 330 K. ESR experiments were performed in a ESP-300 Bruker spectrometer at a microwave frequency of 9.4 GHz in the temperature range 220–570 K. Angular variations of the spectra were measured in different crystallographic planes. dc-susceptibility measurements were performed in a superconducting quantum interference device magnetometer below 300 K and in a Faraday balance magnetometer from 300 to 800 K.

B. Crystal structure and orientation

$\mathrm{La}_{7/8}\mathrm{Sr}_{1/8}\mathrm{MnO}_3$ forms in a rhombohedral $R\overline{3}c$ phase that is preserved down to $T_R \approx 475$ K. Below T_R, a *Pbnm* orthorhombic structure develops, with room-temperature cell parameters[6] $a = 5.5448(2)$ Å $b = 5.5258(2)$ Å, and $c = 7.7927(3)$ Å.

The task of orienting our crystal was achieved by extracting information from both dilatometry and precession camera x-ray-diffraction experiments. There were three main steps in the process, identification of the c axis, identification of a and b axes, and characterization of twinning, described as follows:

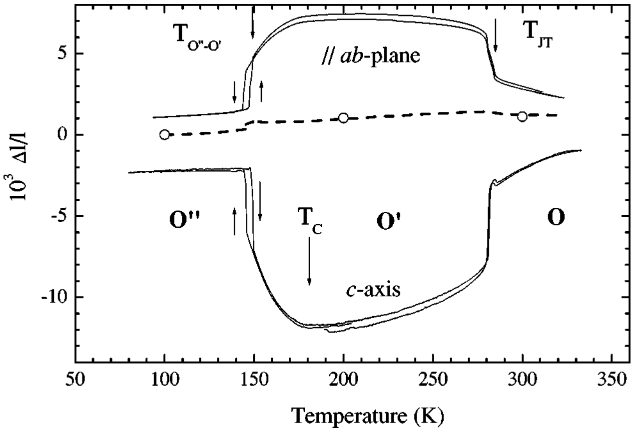

FIG. 1. Thermal expansion vs temperature (solid lines). Measurements were made along the edges in the ab plane and along the c axis. The dashed line indicates the dependence of $\langle a_{av} \rangle = (abc/\sqrt{2})^{1/3}$vs T. All values are *relative* to the value at 100 K (see text).

(1) The *c axis* was identified through dilatometry measurements between 80 K and 350 K. Neutron-diffraction studies[6,13] had shown that in samples of similar composition ($\mathrm{La}_{7/8}\mathrm{Sr}_{1/8}\mathrm{MnO}_3$ and $\mathrm{La}_{0.87}\mathrm{Sr}_{0.13}\mathrm{MnO}_3$), the temperature dependence of the c-cell parameter is signaled by an important contraction ($\sim 1\%$) between 150 and 200 K when T decreases through T_{JT}. We measured thermal expansion $\Delta l/l$ along different directions in the sample (Fig. 1). It was then straightforward to identify the c axis as the direction parallel to the shortest edge of the sample. We confirmed this fact by precession camera x-ray-diffraction experiments.

(2) The a and b axes were identified using the precession camera method. We used this method because back reflection Laue patterns were difficult to interpret due to the twin structure of the samples. From the analysis of the precession camera patterns we determined that a and b axes are parallel to the larger and medium edges of the crystal but it was not possible to distinguish between a and b within the experimental resolution.

(3) Characterization of the twin structure: dilatometry measurements showed the same values for $\Delta l/l$ along the two directions associated with a and b, and the same occurred for the two diagonals in the ab plane. However, since the a and b lattice parameters have different T dependence across T_{JT},[6,13] the crystal is expected to expand along the b-axis, remaining almost unchanged along the a axis. The expansion along b should be similar in magnitude to the contraction along c. In our crystal, the observed expansion in the ab plane is isotropic and about 50% of the contraction in the c direction. Therefore, we conclude that twinning is present in this plane with almost equal proportions of a and b oriented grains. Thus, the curve shown for the ab plane should be considered as an average of a $\Delta a/a$ and $\Delta b/b$. Notice that the contraction along the c axis observed in the dilatometry experiments is somewhat larger than expected on

the basis of neutron-diffraction measurements of the c parameter.[6,13] Thus, if there is twinning in the ac and bc planes it should be small. This twinning structure, with a well determined c axis, has also been observed in Ref. 14.

Our precession camera experiments show also a much less intense secondary x-ray pattern that we associate with minority orientation domains, whose twinning plane is (112). These domains have their c' axes oriented along the ab diagonals of the main structure, and a' and b' axes making an angle of 45° with the c axis. Notice that there are six orientations of this kind in the crystal.

C. Dilatometry

We show in Fig. 1 the detailed T dependence of the thermal-expansion measurements in the ab plane and along the c axis. Here, the relative positions of both curves were fixed in a way that, at 100 K, their separation equals

$$\frac{[(a+b)/2-c/\sqrt{2}]}{\langle a_{av}\rangle}, \tag{1}$$

where $\langle a_{av}\rangle=(abc/\sqrt{2})^{1/3}$ is the geometrically averaged lattice parameter. In the figure, the dashed line indicates the dependence of $\langle a_{av}\rangle$ vs T, *relative* to the value at 100 K. The circles correspond to neutron-diffraction results.[6]

In addition to the valuable information regarding the orientation of the crystal, there are other interesting features inferred from the thermal-expansion results, given as follows.

(i) A very sharp Jahn-Teller transition at $T_{JT}=282$ (3) K, with negligible thermal hysteresis, shows an expansion in the ab plane and a contraction along the c axis when increasing temperature. Previous neutron-diffraction experiments, performed in crushed crystalline ingots[6] and in polycrystalline samples,[13] showed broader transitions centered at about the same temperature.

(ii) The thermal expansion is anomalous well above T_{JT} since the rates of variation are large, as compared with the behavior of other manganites in the paramagnetic regime.[12] The changes observed at T_{JT} continue smoothly up to at least 340 K. This suggests that the crystal is still distorted above T_{JT} and a progressive relaxation takes place towards a more cubic structure, which is stable at higher temperatures. This observation is in agreement with the results of pulsed neutron diffraction[3] that indicate that the microscopic atomic structure in $La_{1-x}Sr_xMnO_3$ deviates significantly from the average structure, with local JT distortions even in non-JT phases.

(iii) Below T_{JT} a slow T evolution of the distortion is also observed.

(iv) Magnetic order at $T_C\sim180$ K is signaled by a change in the sign of $\partial/\partial T$ $(\Delta l/l)$ and the second structural transition to the FM insulating phase O'' was observed at $T_{O''-O'}=147(2)$ K, this time with a noticeable hysteresis of ≈ 3 K.

(v) The crystallographic transition at $T_{O''-O'}$ is accompanied by a large anomaly in $\langle a_{av}\rangle$ that signals a discontinuous volume change.

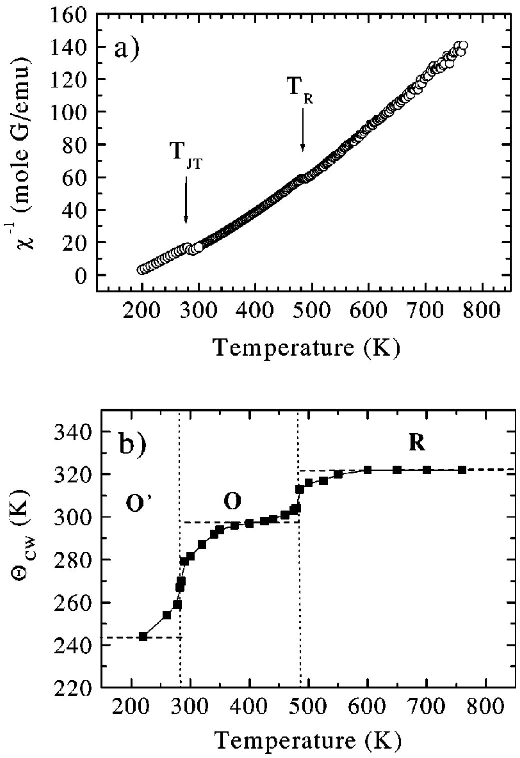

FIG. 2. (a) Inverse of the susceptibility χ^{-1} vs temperature. (b) Θ^{cw} vs temperature, extrapolated as explained in the text. The transition temperatures T_{JT} and T_R are indicated with arrows.

D. dc susceptibility

In Fig. 2(a) we show the inverse of the dc susceptibility, $\chi^{-1}(T)$ vs temperature, which is almost isotropic (variations are less than 4%). The Jahn-Teller and the orthorhombic to rhombohedral structural transitions are clearly featured at $T_{JT}=280(5)$ K and $T_R=480(10)$ K, respectively. They determine three regions: below T_{JT}, between T_{JT} and T_R, and above T_R. For $T\gg T_R$, there is a well-defined Curie-Weiss (CW) behavior with $C=3.15(10)$ emu K/mole G and $\Theta^{\mathrm{CW}}=322(5)$. Below T_R, and especially at the lower temperatures, a positive curvature of $\chi^{-1}(T)$ vs T reproduces the behavior of other CMR manganites,[15] which has been associated with short-range order effects. On the other hand, the two anomalies observed at T_R and T_{JT} may be interpreted in terms of changes of Θ^{CW} accompanying the structural transitions. In lightly doped $LaMnO_{3+\delta}$, which shows strong JT effects, the regions well below and well above T_{JT} were characterized[7] in terms of two different values for Θ^{CW} and a common value for C (and hence the effective magnetic moment). Under the hypothesis that C remains constant for all temperatures, the intermediate T region was described[7] by a temperature dependent $\Theta^{\mathrm{CW}}(T)$. This variation of $\Theta^{\mathrm{CW}}(T)$ was assumed[7] to reflect the changes in the superexchange interactions due to the evolution of the lattice distortions. By analogy, we could try here to identify three different CW temperatures, associated with each crystallographic phase. For this purpose, we should first separate the short-range order effects that originate deviations (positive curvature) from a pure CW behavior. We fitted our experimental data to

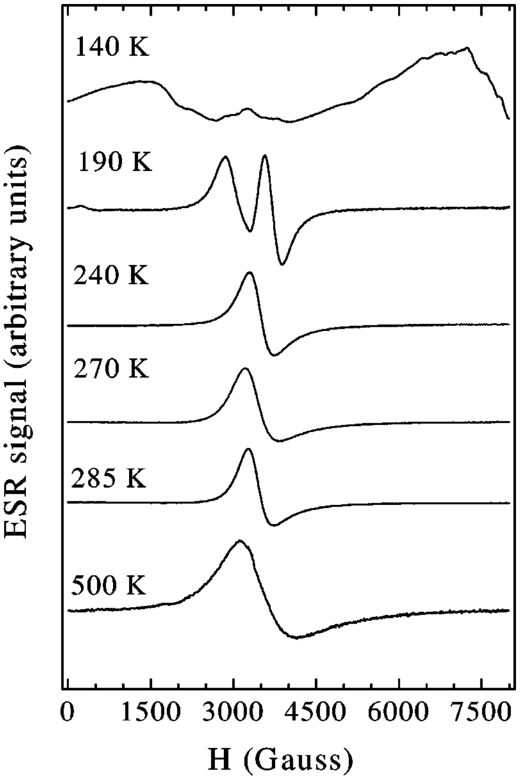

FIG. 3. Normalized ESR spectra at different temperatures. The static magnetic field **H** is parallel to the [100] direction.

an appropriate ($La_{2/3}Sr_{1/3}MnO_3$) normalized susceptibility curve, assuming that the reference compound describes adequately the short-range order effects,[15] at least in a first approximation. In this way, we derived $\Theta_O^{CW} \approx 296(7)$ K and $\Theta_{O'}^{CW} \approx 255(10)$ K for the O and O' phases respectively.

We observed that the fitting with a single Θ^{CW} for each phase shows systematic deviations near the crystallographic transitions. At this point, and following the procedure used for $LaMnO_{3+\delta}$, we determined a T-dependent $\Theta^{CW}(T)$ shown in Fig. 2(b). At the highest temperatures (R-phase) $\Theta^{CW}(T)$ remains almost constant. Two well-defined jumps $\Delta\Theta_{O-R}^{CW} \approx 10$ K and $\Delta\Theta_{O'-O}^{CW} \approx 20$ K appear at T_R and T_{JT}, respectively. Note that the CW temperature increases as the structure evolves towards a more cubic state, reflecting a growth of the ferromagnetic interactions, as in the case[7] of $LaMnO_{3+\delta}$. Above and below the sharp jump at T_{JT} that signals the suppression of the cooperative JT distortions, $\Theta^{CW}(T)$ varies smoothly with temperature, resembling the T dependence of the thermal expansion (see Fig. 1). This similarity indicates that the variations of $\Theta^{CW}(T)$ are indeed associated with the evolution of the crystalline parameters.

The effective magnetic moment $\mu_{eff} = 5.02\ \mu_B$, derived from the C constant measured at high temperatures (up to 800 K) is another interesting feature of the dc susceptibility of $La_{7/8}Sr_{1/8}MnO_3$. The positive curvature of $\chi^{-1}(T)$ at lower temperatures may be described as an increasing magnetic moment. As in Refs. 16 and 17, dc-susceptibility measurements up to $T \approx 350$ K show apparent values of $\mu_{eff} \approx 6.5\mu_B$. These high values were interpreted by Nogues *et al.*[18] in terms of the existence of magnetic clusters where a hole is shared by several Mn ions. Our measurements show that the apparent moment changes in a continuous way as the temperature increases, suggesting that the assumed cluster structure evolves with temperature. At high temperatures the apparent moment decreases down to $5.02\mu_B$, which is still larger than the average expected for an appropriate mixture of Mn^{3+} and Mn^{4+} free ions, $\mu_{eff}^{av} = 4.78\mu_B$. A Curie-Weiss law with a C constant different from the free-ion theoretical value has been observed in several manganites[15,19] where localized moments strongly interact with itinerant electrons. This behavior has been modeled,[20] in a mean-field approximation, for the case of the double-perovskite Sr_2FeMoO_6, where well-localized Fe^{3+} ions interact antiferromagnetically with delocalized electrons. The resulting C constant is given by $C = C_0(1+\lambda\chi_e^0)^2$, where C_0 is the free-ion value,

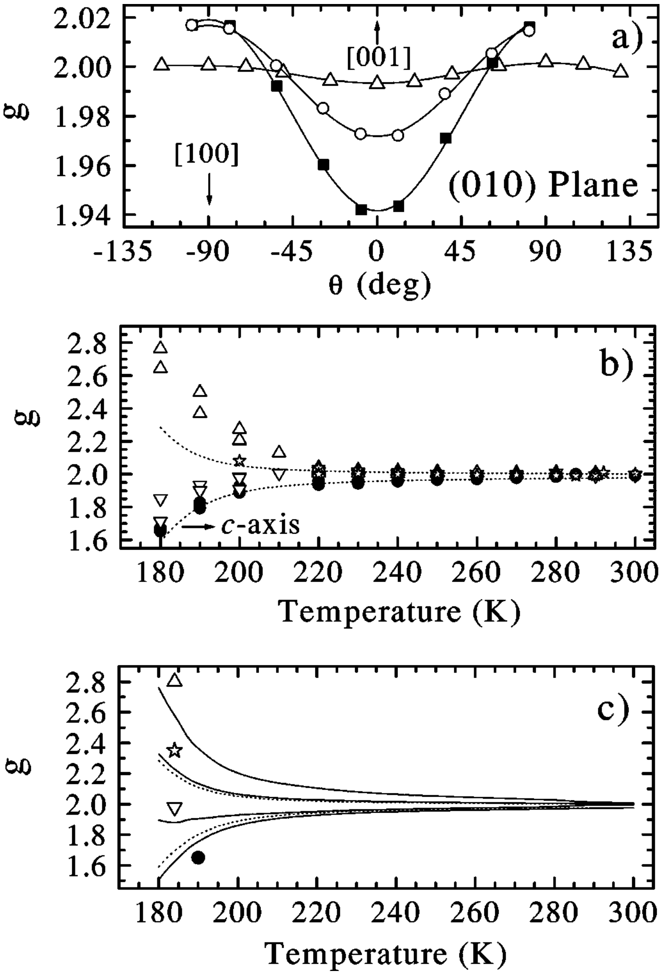

FIG. 4. (a) Angular variation of the effective g factor in the (010) plane for different temperatures: 220 K (filled squares), 250 K (circles), and 300 K (triangles). (b) Experimental effective g factor vs temperature for fixed orientations of the sample: H // [100] (down triangles), H // [010] (up triangles), H // [110] (stars), and H// [001] (circles). The dashed lines are calculated g-factor values in the ab plane and along the c axis including demagnetizing field effects. (c) Solid lines: calculated g-factor values including *both* demagnetizing field and crystal field corrections. Symbols and dashed lines: the same as in (b).

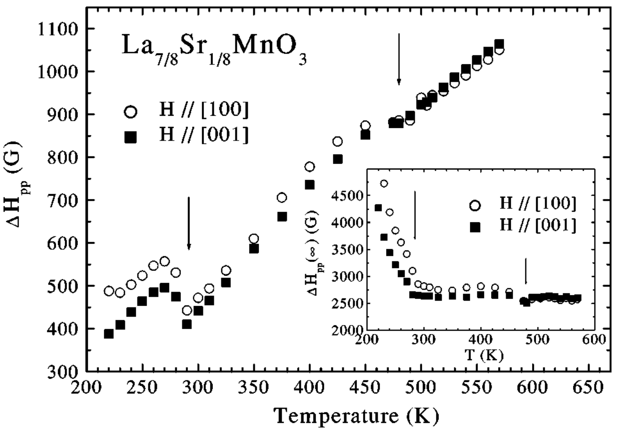

FIG. 5. ΔH_{pp}vs temperature for fixed orientations of the sample: H // [100] (open circles) and H // [001] (filled squares). Inset: idem for $\Delta H_{pp}^{(\infty)}$. The T_{JT} (282 K) and T_R transitions are indicated with arrows.

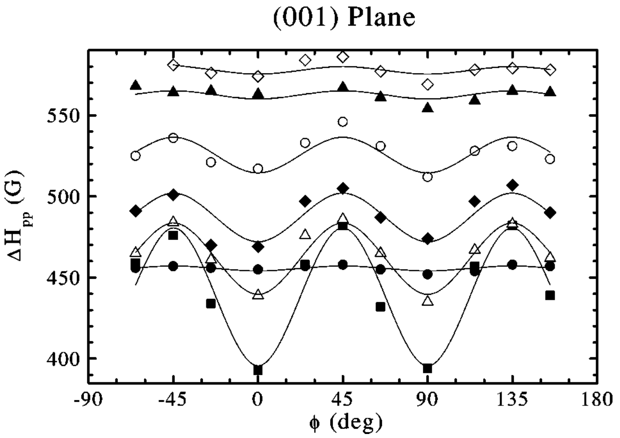

FIG. 6. Angular variation of ΔH_{pp} in the (001) plane for different temperatures: 220 K (squares), 230 K (open triangles), 240 (filled diamonds), 250 K (empty circles), 270 K (open diamonds), 280 K (filled triangles), and 290 K (filled circles).

λ is the coupling parameter, and χ_e^0 is a temperature-independent susceptibility associated with the itinerant electrons. In the case of electron doped $Ca_{1-x}Y_xMnO_3$, where $\lambda > 0$ corresponds to a FM coupling, an enhanced C constant was measured.[19] For $La_{7/8}Sr_{1/8}MnO_3$, λ is also FM and a similar mechanism may explain our observation of a larger magnetic moment. Monte Carlo simulations[19] for lightly electron doped $CaMnO_3$ have shown that at high T the electrons are highly delocalized and as T_C is approached begin to localize forming magnetic polarons. This picture may apply to our case, describing the T evolution of the apparent magnetic moment.

E. Electron-spin resonance

ESR studies were carried out in the paramagnetic regime from 220 K to 580 K, well above T_C. The ESR spectrum consists of a single Dysonian line (mix of absorption and dispersion). In Fig. 3 we present selected ESR spectra at different temperatures. Above T_{JT}, the g factor is approximately isotropic and temperature independent with an average value $g = 1.997(3)$ after correcting for the dispersion component. For $T < T_{JT}$, the g becomes anisotropic, as shown in Fig. 4(a) for **H** in the (010) plane at different temperatures. The anisotropy decreases with increasing temperature, as seen in Fig. 4(b), where we plot the g factor for the crystallographic directions a, b, c, and ab diagonal ([110]).

The peak-to-peak linewidth ΔH_{pp} is also anisotropic. The temperature dependence of ΔH_{pp} for a fixed orientation of the sample is shown in Fig. 5 for **H** // [100] and **H** // [001]. When raising the temperature, the Jahn-Teller transition is clearly signaled at $T_{JT} \approx 285$ K by a decrease of $\Delta H_{pp}(T)$, similar to that observed previously[1,4] for $LaMnO_3$ and several compositions of $La_{1-x}Sr_xMnO_3$. A second step indicates the structural transition from the orthorhombic O to the rhombohedral $R\bar{3}c$ phase at $T_R = 480$ K, followed by a further reduction of the anisotropy above T_R. The ESR linewidth presents, at all temperatures, an angular dependence similar to that we previously reported[8,9] for $T = 220$ K. The ESR linewidth is maximum for **H** // [100] and minimum along the [001] direction with a 180° periodicity in the (010) and (100) planes. In the diagonal planes (110) and $(\bar{1}10)$ the periodicity is also 180°. Instead, 90° symmetry was observed for **H** in the (001) plane. In Figs. 6 and 7, the angular variations for different temperatures up to 350 K in the (001) and (010) planes are shown. The anisotropy decreases with

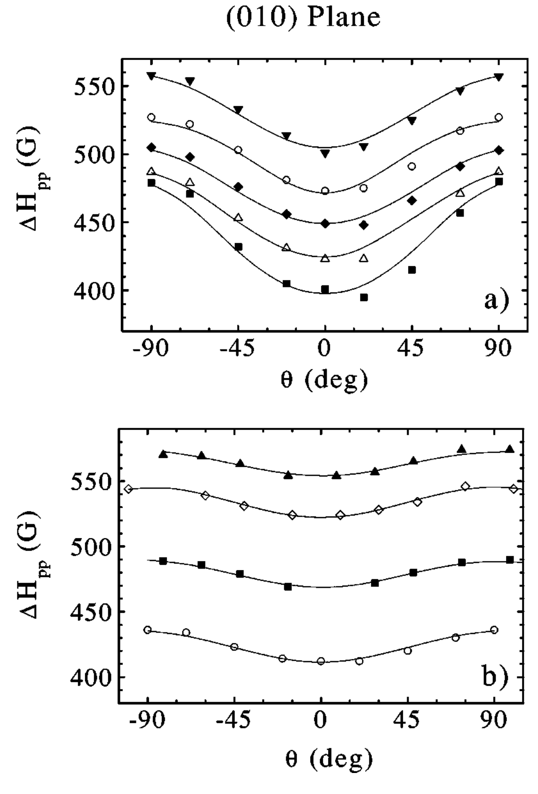

FIG. 7. Angular variation of ΔH_{pp} in the (010) plane for different temperatures. (a) 220 K (squares), 230 K (open triangles), 240 (filled diamonds), 250 K (open circles), and 270 K (filled triangles). (b) 290 K (circles), 310 K (squares), 330 K (diamonds), and 340 K (triangles).

increasing temperature and becomes very small above T_{JT}. However, it does not disappear completely and presents an appreciable value (≈ 50 G) up to about 450 K. Above T_R the linewidth becomes isotropic.

The temperature dependence of $\Delta H_{pp}(T)$ is determined, to a large extent, by the variations of $\chi(T)$ and is given by[15]

$$\Delta H_{pp}(T)=[C/T\chi(T)]\Delta H_{pp}(\infty), \tag{2}$$

where ΔH_{pp} (∞) is identified with the linewidth extrapolated to high temperatures. Although this parameter is usually expected to be temperature independent, ΔH_{pp} (∞) does depend on the structural properties of the system (e.g., crystal structure, local distortions, ionic distances, etc.), which may change with temperature.[16] From the experimental $\Delta H_{pp}(T)$ and the measured $\chi(T)$ we obtained $\Delta H_{pp}(\infty)$ at each temperature and for different orientations of **H**, using Eq. (2). The results are shown in the inset of Fig. 5. This procedure separates the effects of the thermodynamic factor $C\ /T\chi(T)$, responsible for the average increase of $\Delta H_{pp}(T)$ in the paramagnetic region, from the variations of the intrinsic parameter $\Delta H_{pp}(\infty)$. It is interesting to note the important decrease of $\Delta H_{pp}(\infty)$ as the symmetry of the lattice increases with temperature, with the crystallographic transitions featured by two steps at T_{JT} and T_R (see the arrows in the inset of Fig. 5). As discussed in the following section, $\Delta H_{pp}(\infty)$ involves the microscopic parameters associated with the spin Hamiltonian of the system.

The angular dependence of the measured $\Delta H_{pp}(T)$ is mainly related to $\Delta H_{pp}(\infty)$ since the dc-susceptibility anisotropy is very small (negligible in the ab plane and less than 4% out of this plane). The experimental data were fitted for each temperature to the following expression, appropriated for the observed tetragonal symmetry:

$$\Delta H_{pp}(\infty)\propto\alpha(T)+\beta(T)(3\cos^2\theta-1)+\gamma(T)(35\cos^4\theta$$
$$-30\cos^2\theta+3)+\delta(T)\sin^4\theta\cos 4\varphi. \tag{3}$$

The angles θ and φ give the orientation of the magnetic field **H** with reference to the crystal axes ($\varphi=0$ for **H** // [110]). The first fitting showed that in the whole temperature range, $\gamma(T)<1G$, thus we set $\gamma=0$ within our experimental resolution. From the amplitude of the angular variation in the (001) plane ($\theta=\pi/2$) we were able to determine $\delta(T)$. The remaining parameters $\alpha(T)$ and $\beta(T)$ were adjusted by fitting the data in the (010) and $(\bar{1}10)$ planes, using the value of $\delta(T)$ previously determined. This procedure was repeated between 220 K and 450 K and the results are shown in Fig. 8.

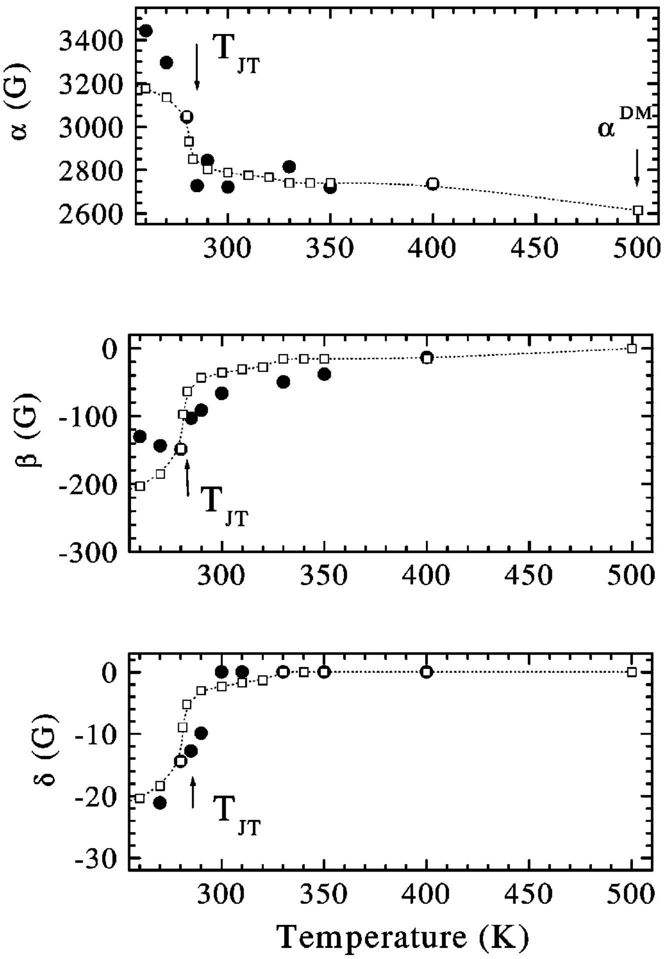

FIG. 8. ESR linewidth parameters α, β, and δ vs temperature: (i) from the fitting of ESR data (open symbols) and (ii) as calculated (see text) from the model and the thermal expansion results (filled squares). The lines are guides to the eye.

III. ESR PARAMETERS AND SPIN HAMILTONIAN

An approach to the description of the angular variation of the ESR spectrum can be based on Kubo and Tomita's scheme[21,22] to model the response of a magnetic system under the excitation produced by a linearly polarized microwave field of frequency ω. The imaginary part of the dynamical susceptibility $\chi''(\omega,H)$ per unit of volume for $k_BT \gg \hbar\omega$ is given by[23,24]

$$\chi''(\omega,B)=\frac{\omega V}{2k_BT}\int_{-\infty}^{\infty}\langle M_{h_1}(t,H)M_{h_1}\rangle\exp(-i\omega t)dt, \tag{4}$$

where $\mathbf{H}=H\hat{\mathbf{h}}$ is the external magnetic field along $\hat{\mathbf{z}}$ and $\hat{\mathbf{h}}_1$ is the polarization direction of the microwave field. M_{h_1} is the component of the magnetization operator along $\hat{\mathbf{h}}_1$ and

$$M_{h_1}(t,H)=\exp[i/\hbar\mathcal{H}(H)\ t]M_{h_1}\exp[-i/\hbar\mathbf{M}(H)t], \tag{5}$$

with $\mathcal{H}(H)$ being the Hamiltonian of the system and $\langle\mathbf{A}\rangle \equiv \mathrm{Tr}\{\rho\mathbf{A}\}$, where ρ is the density matrix operator.

The complete Hamiltonian for the system reads

$$\mathcal{H}=\mathcal{H}_Z+\mathcal{H}_{exch}+\mathcal{H}_{CF}+\mathcal{H}_{DM}, \tag{6}$$

where $\mathcal{H}_Z$, $\mathcal{H}_{exch}$, $\mathcal{H}_{CF}$, and $\mathcal{H}_{DM}$ represent the Zeeman, the Heisenberg exchange, the single-site crystal field (CF), and the Dzyaloshinsky-Moriya interactions, respectively. Taking into account that the system includes k nonequivalent magnetic ions per unit cell ($k=4$ in the O and O' phases, and $k=2$ in the R phase), these contributions can be written as

$$\mathcal{H}_Z=\mu_B H\sum_{i=0}^{N}\sum_{p=1}^{k}\vec{\mathbf{S}}(ip)\mathbf{g}(p)\hat{\mathbf{h}},\tag{7a}$$

$$\mathcal{H}_{exch}=1/2\sum_{i,j=0}^{N}\sum_{p,q=1}^{k}J(ip,jq)[\vec{\mathbf{S}}(ip)\cdot\vec{\mathbf{S}}(jq)],\tag{7b}$$

$$\mathcal{H}_{CF}=\sum_{i=0}^{N}\sum_{p=1}^{k}\vec{\mathbf{S}}(ip)\mathbf{D}(p)\vec{\mathbf{S}}(ip),\tag{7c}$$

$$\mathcal{H}_{DM}=1/2\sum_{i,j=0}^{N}\sum_{p,q=1}^{k}\mathbf{d}(ip,jq)\cdot[\vec{\mathbf{S}}(ip)\times\vec{\mathbf{S}}(jq)].\tag{7d}$$

The sum over p (or q) runs over the different magnetic ion sites (1-k) in the unit cell, while i (or j) sums over the N unit cells of the crystal. One might also add dipole-dipole interaction terms, but an order of magnitude estimation indicates that these are less important. Since the operators involved in Eqs. (7a)–(7d) are mutually noncommuting, the computation of Eqs. (4) and (5) requires a perturbational approach. According to Eq. (7a), if all the magnetic ions in the unit cell were magnetically nonequivalent, one would expect a set of four lines for a general orientation of the crystal with reference to the external field direction. However, the observed spectrum exhibits, for $T>200$ K, only one line for any orientation of the crystal. This is an indication that the exchange narrowing process is under operation leading to a collapsed spectra. Thus, the isotropic exchange ($|J|/k_B\simeq 25$ K) will be assumed to be the strongest interaction. On the other hand, one may observe that $\mathcal{H}_Z$ can be written as

$$\mathcal{H}_Z=\mu_B H\ \vec{\mathbf{S}}\mathbf{g}_{av}\ \hat{\mathbf{h}}+\mathcal{H}_{Zres},$$

with

$$\mathbf{g}_{av}=\frac{1}{k}\sum_{p=1}^{k}\mathbf{g}(p)$$

and $\vec{\mathbf{S}}$ being the total spin operator. The residual Zeeman interaction $\mathcal{H}_{Zres}$ sometimes becomes a source of field-dependent perturbation, particularly for moderate anisotropies of the $\mathbf{g}(p)$ tensors and small exchange interactions.[25] However, in our case for experiments performed at X band, these contributions can be ignored. Furthermore, the small anisotropy observed for $\mathbf{g}_{av}$ allows one to replace $\mathbf{g}_{av}\simeq g\,\mathbf{1}$. Therefore, the unperturbed Hamiltonian will be

$$\mathcal{H}_0\simeq\mu_B gHS_z+\mathcal{H}_{exch},\tag{8}$$

where the quantization axis $\hat{\mathbf{z}}$ is along $\hat{\mathbf{h}}$, and the excitation field $\hat{\mathbf{h}}_\mathbf{1}$ is along $\hat{\mathbf{x}}$. The perturbing Hamiltonian is then

$$\mathcal{H}'=\mathcal{H}_{CF}+\mathcal{H}_{DM}.\tag{9}$$

The density matrix may be approximated by $\rho\simeq 1/\mathrm{Tr}\{\mathbf{1}\}\times[\mathbf{1}-1/kT\mathcal{H}_{exch}-(\hbar\omega_o/kT)S_z]$ although in this section it will be taken in the high-temperature approximation: $\rho\simeq\mathbf{1}/\mathrm{Tr}\{\mathbf{1}\}$, widely justified in the paramagnetic regime. Thus, the calculated linewidth corresponds effectively to $\Delta H_{pp}(\infty)$ in Eq. (2), though we will not use the symbol (∞) in the following subsection.

With these prescriptions we followed standard approximation procedures as summarized in Appendix A. In this approximation for the density matrix, the ESR line is centered at $H_R=\hbar\omega_o/g\mu_B$. Higher-order contributions will be discussed in following sections.

Up to second order in $\mathcal{H}'$ we found that both the CF and DM interactions contribute separately to the resonance field and linewidth.

A. Linewidth

The angular dependence of the linewidth is given by

$$\Delta H(\theta,\varphi)=\Delta H^{CF}(\theta,\varphi)+\Delta H^{DM}(\theta,\varphi).$$

$\Delta H^{CF}(\theta,\varphi)$ is built up from three terms

$$\Delta H^{CF}(\theta,\varphi)=\Delta H^{CF}_{\mathrm{sec}}(\theta,\varphi)+\Delta H^{CF}_{ns(1)}(\theta,\varphi)+\Delta H^{CF}_{ns(2)}(\theta,\varphi),\tag{10}$$

where sec stands for secular, and ns(1) and ns(2) for nonsecular contributions that correspond to terms involving factors such as $\exp(\pm i\omega_o\tau)$ and $\exp(i2\omega_o\tau)$, respectively. Explicit expressions for the terms in Eq. (10) are

$$\Delta H^{CF}_{\mathrm{sec}}(\theta,\varphi)=(f_0/\omega_{exch})\sum_{p=1}^{k}[3\mathbf{D}_{zz}(p)-\mathrm{Tr}\,\mathbf{D}(p)]^2,\tag{11a}$$

$$\Delta H^{CF}_{ns(1)}(\theta,\varphi)=(f_1/\omega_{exch})\sum_{p=1}^{k}[(\mathbf{D}^2(p))_{zz}-(\mathbf{D}_{zz}(p))^2],\tag{11b}$$

$$\begin{aligned}\Delta H^{CF}_{ns(2)}(\theta,\varphi)=(f_2/\omega_{exch})\sum_{p=1}^{k}\{&2[\mathbf{D}_{zz}(p)]^2-4[\mathbf{D}^2(p)]_{zz}\\&+2\,\mathrm{Tr}(\mathbf{D}^2(p))-[\mathbf{D}_{zz}(p)-\mathrm{Tr}\,\mathbf{D}(p)]^2\},\end{aligned}\tag{11c}$$

with $\mathbf{D}_{zz}$ referred to the system with $\hat{\mathbf{z}}$ // $\mathbf{H}$, and $\omega_{exch}=\sqrt{zJ^2/\hbar^2}$ being an average of the superexchange interactions J, taken over the z first nearest neighbors of the magnetic ion. In arriving to Eqs. (11a)–(11c) we have taken into consideration the periodic properties of the crystal lattice. We have assumed that the spin self-correlation functions have a fast decay with Gaussian shape. If, additionally, they are identical, the weight factors f_0, f_1, and f_2 are

$$f_0=f_2=\frac{1}{10g\mu_B\hbar}\sqrt{\frac{2\pi}{3}}[S(S+1)-3/4],\tag{12a}$$

$$f_1=\frac{5}{10g\mu_B\hbar}\sqrt{\frac{2\pi}{3}}[S(S+1)-3/4].\tag{12b}$$

Similarly (see Appendix A), the DM contribution has the form

$$\Delta H^{DM}(\theta,\varphi)=\frac{f_{DM}}{\omega_{exch}}\sum_{\alpha\neq\beta}\sum_{j=0,N}[\mathbf{d}(0\alpha,j\beta)\cdot\hat{\mathbf{z}}]^2 \quad (13)$$

with

$$f_{DM}=\frac{1}{g\mu_B\hbar}\sqrt{\frac{\pi}{108}}[S(S+1)(2S+1)^2].$$

B. The line position

By taking $\rho\simeq 1/\mathrm{Tr}\{\mathbf{1}\}$ in the preceding section, both $\mathcal{H}_{exch}$ and the Zeeman interaction were absent from the density matrix. Returning now to the first-order contribution as given by Eq. (A4) in Appendix A, and including only the Zeeman term in the density matrix as

$$\rho\rightarrow\rho'\simeq\rho\left(\mathbf{1}-\frac{\hbar\omega_o}{kT}S_z\right).$$

Then, in Eq. (A4), the linear terms in $\tilde{\mathcal{H}}'$ lead to

$$\delta_u(t)\simeq -u\frac{\omega_o}{2k_BT}\int_0^t d\tau\frac{1}{\langle S_z^2\rangle}$$
$$\times\mathrm{Tr}\left\{\rho\tilde{\mathcal{H}}'(\tau)\left(S_z^2-\frac{1}{2}(S_uS_{-u}-S_u^2)\right)\right\}.$$

Note that, as $\mathcal{H}_{exch}$ commutes with all the components of the total spin operator, it follows

$$\left[\mathcal{H}_{exch},\left(S_z^2-\tfrac{1}{2}(S_{\mp}S_{\pm}-S_{\mp}S_{\mp})\right)\right]=0.$$

If we take $\mathcal{H}'\equiv\mathcal{H}_{CF}$ we obtain an angular dependent position of the ESR line at $H_R=\hbar\omega_o^{eff}(\theta,\varphi)/g\mu_B$, where (see Appendix A)

$$-u\omega_ot+\delta_u(t)=-u\omega_o^{eff}(\theta,\varphi)t.$$

This result may be expressed in terms of an effective g value, $g^{eff}(\theta,\varphi,T)$, given by

$$g^{eff}(\theta,\varphi,T)=g\left\{1-(1/20k_BT)[S(S+1)-3/4]\right.$$
$$\left.\times\sum_{p=1}^{k}[3\mathbf{D}_{zz}(p)-\mathrm{Tr}\,\mathbf{D}(p)]\right\}. \quad (14)$$

Thus, the overall angular variation of the exchange collapsed line position results from a superposition of the individual k-site angular variation contributions. The DM term in $\mathcal{H}'$ does not contribute to the line shift.

C. Crystal field detailed calculation

For the *Pbnm* phase, the components of $\mathbf{D}(p)$ in Eq. (7c), referred to the crystalline axes, are related by symmetry properties

p	$(\xi\xi)$	$(\eta\eta)$	$(\varsigma\varsigma)$	$(\xi\eta)$	$(\xi\varsigma)$	$(\eta\varsigma)$
1	$-D$	$-E_2$	E_1	$\frac{1}{2}G$	$\frac{1}{2}F_1$	$\frac{1}{2}F_2$
2	$-E_2$	$-D$	E_1	$\frac{1}{2}G$	$\frac{1}{2}F_2$	$\frac{1}{2}F_1$
3	$-E_2$	$-D$	E_1	$\frac{1}{2}G$	$-\frac{1}{2}F_2$	$-\frac{1}{2}F_1$
4	$-D$	$-E_2$	E_1	$\frac{1}{2}G$	$-\frac{1}{2}F_1$	$-\frac{1}{2}F_2$

(15)

We have chosen ς along the c axis, and the $\xi\eta$ plane coincident with the ab plane, with ξ in the direction of the Mn-O bond.

By applying the rules of transformation of spin operators we obtain the following CF contribution to the coefficients in Eq. (3):

$$\alpha^{CF}=\frac{f_0}{\omega_{exch}}\alpha_{\mathrm{sec}}^{CF}+\frac{f_1}{\omega_{exch}}\alpha_{ns(1)}^{CF}+\frac{f_2}{\omega_{exch}}\alpha_{ns(2)}^{CF} \quad (16)$$

and similar formulas for β^{CF}, γ^{CF}, and δ^{CF}. These coefficients can be written in terms of the crystal field Hamiltonian parameters, i.e,

$$\alpha_{\mathrm{sec}}^{CF}=\tfrac{252}{35}A^2+\tfrac{84}{35}(B^2+G^2+F^2), \quad (17a)$$

$$\beta_{\mathrm{sec}}^{CF}=\tfrac{36}{7}A^2-\tfrac{12}{7}(G^2+B^2)+\tfrac{6}{7}F^2, \quad (17b)$$

$$\gamma_{\mathrm{sec}}^{CF}=\tfrac{81}{35}A^2+\tfrac{9}{70}(G^2+B^2)-\tfrac{18}{35}F^2, \quad (17c)$$

$$\delta_{\mathrm{sec}}^{CF}=\tfrac{9}{2}(B^2-G^2), \quad (17d)$$

where $A=1/3(D+2E_1+E_2)$, $B=E_2-D$, and $F^2=F_1^2+F_2^2$. Similar expressions arise for the nonsecular contributions (see Appendix B).

We note that extra terms are also present, arising because of the orthorhombic symmetry of the crystal structure:

$$\varepsilon_{\mathrm{sec}}^{CF}(\theta,\varphi)=-18[\cos^4\theta(2F_1F_2+3AG)$$
$$-\cos^2\theta(4AG+2F_1F_2)+AG]\sin 2\varphi \quad (18)$$

and their corresponding nonsecular terms.

The result obtained corresponds to a perfect single crystal. The final expression appropriate to our twinned crystal should take into account all the possible orientations. In what follows we assumed that the contributions to the linewidth originating in different orientation domains of the sample can be arithmetically averaged. This is a good approximation when the linewidths are similar and the resonance fields differ by much less than the linewidth. When we take into account the six possible orientations, we have to replace in Eqs. (17a)–(17d), and (18)

$$\alpha^{CF}\rightarrow\alpha^{CF}, \quad (19)$$

$$\beta^{CF}\rightarrow\beta^{CF}(1-3m_t), \quad (20)$$

$$\gamma^{CF}\rightarrow\left(1-\frac{5}{4}m_t\right)\gamma^{CF}+\frac{1}{4}\delta^{CF}m_t, \quad (21)$$

$$\delta^{CF}\rightarrow\frac{35}{4}m_t\gamma^{CF}+\left(1-\frac{7}{4}m_t\right)\delta^{CF}, \quad (22)$$

$$\varepsilon^{CF} \to 0. \tag{23}$$

These expressions have been derived under the assumption that the four minority orientations (two different c axes with two associated 90° rotated domains) *are present in the same proportion*, m_t. The two main orientations have a weight factor M_t, such that $M_t + 2m_t = 1$. Notice that the $\varepsilon^{CF}(\theta,\varphi)$ term cancels out, independent of the value of m_t, and the full spectrum has then tetragonal symmetry.

For the $R\overline{3}c$ phase, the local symmetry for Mn ions is O_h, and the second-order crystal field coefficients vanish.

D. Dzyaloshinsky-Moriya detailed calculation

Computing only first neighbor interactions in Eq. (13) we observe that the terms of the type $f(\cos 2\varphi, \sin 2\varphi)$ cancel out when twinning is considered, as in the case of crystal field contributions. We obtain then

$$\alpha_{DM} = \left(\frac{4}{3k}\right) \frac{f_{DM}}{\omega_{exch}} \sum_{p=1}^{k} \sum_{r=1}^{6} |\mathbf{d}^{(r)}|^2 = \frac{8 f_{DM}}{\omega_{exch}} \langle |\mathbf{d}|^2 \rangle, \tag{24}$$

$$\beta_{DM} = \left(\frac{2}{3k}\right) \frac{f_{DM}}{\omega_{exch}} \sum_{p=1}^{k} \sum_{r=1}^{6} [3(d_\varsigma^{(p,r)})^2 - |\mathbf{d}^{(r)}|^2] = \frac{4 f_{DM}}{\omega_{exch}} [3\langle d_\varsigma^2 \rangle - \langle |\mathbf{d}|^2 \rangle], \tag{25}$$

$$\gamma_{DM} = \delta_{DM} = 0, \tag{26}$$

where the p sums run over the different lattice Mn sites and the r sums over the corresponding six nearest neighbors (nn); the brackets $\langle\ \rangle$ indicate average values over nn. Independent of the symmetry, $\gamma_{DM} = \delta_{DM} = 0$ results from the mathematical form of Eq. (13). For the DM interaction we observe also that there are no nonsecular contributions to the linewidth.

For the rhombohedral $R\overline{3}c$ phase we have calculated the components of $\mathbf{d}^{(p,r)}$ allowed by the symmetry. We considered the two Mn sites located at $P = (0,0,0)$ and $P' = (0,0,1/2)$, referred to the hexagonal axes $\vec{a}_H = a_0(\hat{x} - \hat{z})$, $\vec{b}_H = a_0(-\hat{x} + \hat{y})$, and $\vec{c}_H = 2a_0(\hat{x} + \hat{y} + \hat{z})$, where a_0 is the cubic perovskite parameter. For the P first neighbors X, Y, and Z located at $a_0\hat{\xi}$, $a_0\hat{\eta}$, and $a_0\hat{\varsigma}$, respectively, we obtained

$$\vec{d}_{PX} = (d_\xi, d_\eta, d_\varsigma) = \vec{d}_{P(-X)}, \tag{27a}$$

$$\vec{d}_{PY} = (d_\varsigma, d_\xi, d_\eta) = \vec{d}_{P(-Y)}, \tag{27b}$$

$$\vec{d}_{PZ} = (d_\eta, d_\varsigma, d_\xi) = \vec{d}_{P(-Z)}, \tag{27c}$$

where $-X$, $-Y$, and $-Z$ indicate the opposite sites. For the corresponding P' neighbors $\vec{d}_{P'X} = (-d_\xi, -d_\varsigma, -d_\eta)$ and the other parameters are obtained by cyclic permutations as for the P site. Thus, for a perfect single crystal in the rhombohedral phase,

$$\Delta H_{DM}(\theta,\varphi) = 8\frac{f_{DM}}{\omega_{exch}}(d_\xi^2 + d_\eta^2 + d_\varsigma^2) + 4\frac{f_{DM}}{\omega_{exch}}(d_\xi d_\eta + d_\eta d_\varsigma + d_\xi d_\varsigma) \times [\sin^2\theta \sin 2\varphi + \sin 2\theta(\sin\varphi + \cos\varphi)]. \tag{28}$$

If we now take into account the four possible orientations for $\hat{c}_H$ in the twinned crystal, all the angular dependences in Eq. (28) vanish and the DM linewidth becomes isotropic.

For the orthorhombic O and O' phases, using the relations between components of the **d** coefficients given by Solovyev *et al.*[26] for the $Pbnm$ symmetry, and taking into account the twinned structure, we derive

$$\alpha_{DM} = \frac{f_{DM}}{3\omega_{exch}}[16(d_\varsigma^{ab})^2 + 16(d_\xi^{c})^2 + 16(d_\eta^{c})^2 + 8(d_\xi^{c})^2 + 8(d_\eta^{c})^2], \tag{29a}$$

$$\beta_{DM} = \frac{f_{DM}}{3\omega_{exch}}(1 - 3m_t)^{-1}[16(d_\varsigma^{ab})^2 - 8(d_\xi^{ab})^2 - 8(d_\eta^{ab})^2 - 4(d_\xi^{c})^2 - 4(d_\eta^{c})^2], \tag{29b}$$

where the suffixes *ab* and *c* refer to components of a DM vector connecting the central ion with in-plane (*ab*) and *c*-axis nearest neighbors, respectively.

IV. DISCUSSION

In this section we will discuss first the behavior of the parameters $\alpha(T)$, $\beta(T)$, and $\delta(T)$ that describe the measured linewidth, considering the different contributions analyzed in the preceeding section.

Above T_R we observed an isotropic and temperature-independent linewidth (see Fig. 5), characterized by a constant α. Note that in this rhombohedral phase β_{DM} is expected to identically vanish, in agreement with our experimental data. On the other hand, no crystal field contributions are expected because the cubic local symmetry does not allow second order terms of the type included in Eq. (7c). Thus, only the DM interaction contributes to the linewidth, and $\alpha(T > T_R) = \alpha_{DM}^{(R)} = 2600(30)G$. From Eq. (24), and using $2830G$ for f_{DM}/ω_{exch}, we derived an average value $\langle |\mathbf{d}|^2 \rangle_R^{1/2}/k_B = 0.34(1)$ K.

For the orthorhombic phases O and O', both the crystal field and the DM interactions add to the linewidth due to the reduction of the local symmetry of the resonant ions. In the O phase, the distortions of the octahedra are significantly smaller than in the O' phase, especially, as we will discuss later, well above the transition temperature, T_{JT}. Thus, we may assume, in a first approximation, that close to T_R the main contribution to the linewidth has a DM origin, as in the case of the R phase. Then,

$$\alpha(T \lesssim T_R) \approx \alpha_{DM}^{(O)} \approx 2750(50)G, \tag{30}$$

$$\beta(T \lesssim T_R) \simeq (1-3m_t)\beta_{DM}^{(O)} \approx -15(5)G. \qquad (31)$$

From Eqs. (29a) and (29b) we obtain $\langle|\mathbf{d}|^2\rangle_O^{1/2}/k_B = 0.35(1)$ K, and $\langle|\mathbf{d}_s^{ab}|\rangle_O/k_B \cong 0.24(1)$ K using $\hbar\omega_{exch}/k_B = 61$ K.

The DM interaction appears because of the tilting of the MnO_6 octahedra, and neutron-diffraction experiments[2,5,13] have shown that the Mn-O-Mn angles remain essentially constant with temperature. Thus, it is not surprising that only a small change is observed across T_R. Following this argument, we may expect that α_{DM} and β_{DM} are almost temperature independent in both phases O and O'. The values of $\alpha_{DM}^{(O)}$ and $\beta_{DM}^{(O)}$ were then subtracted from the measured $\alpha(T)$ and $\beta(T)$ in order to separate the crystal field contributions, α_{CF} (T) and $\beta_{CF}(T)$.

We observe that the measured parameters $\alpha(T)$, $\beta(T)$, and $\delta(T)$ shown in Fig. 8 signal the Jahn-Teller transition with noticeable steps at T_{JT} and approach asymptotic values well above this temperature. In order to correlate the observed T dependence of the ESR parameter anisotropy with the evolution of the distortions of the MnO_6 octahedron, it is convenient to refer the system to a ''local'' coordinates frame defined by its principal axes. Neutron-diffraction results[2,13] indicate that the MnO_6 octahedra present tetragonal $(Q_{3g,u})$ and orthorhombic $(Q_{3g,v})$ distortions from the cubic symmetry, preserving approximately the right angles. The local CF Hamiltonian is then

$$\mathcal{H}_{local}^{CF} = \tilde{D}S_{\tilde{x}}^2 + \tilde{E}(S_{\tilde{y}}^2 - S_{\tilde{z}}^2), \qquad (32)$$

where $\tilde{x}$ and $\tilde{y}$ are the Mn-O directions in the basal plane of the octahedron. Equation (32) corresponds to one Mn site in the unit cell and similar expressions could be readily deduced for the other three sites by applying the symmetry operations of the *Pbnm* group. The parameters $\tilde{D}$ and $\tilde{E}$ are related to the coefficients in Eqs. (7a)–(7d) as shown in Appendix B.

We have analyzed first the results at $T = 280$ K. This temperature is appropriate for the first determination of $\tilde{D}$ and $\tilde{E}$, because the system is already in the JT distorted O' phase and far enough from T_C, where other mechanisms may affect the linewidth. In the fitting we left as adjustable parameters, besides $\tilde{D}$ and $\tilde{E}$, the twinning fraction m_t and the weight factors f_1 and f_2 [leaving f_0 as given by Eq. (12a)]. We found the best fit with a ratio $f_0:f_1:f_2$ equal to 1:10:0.3 instead of the ratio 1:5:1 predicted by Eqs. (12a) and (12b) that rests heavily on the hypothesis that all the spin correlation functions are equal. This assumption, although considerably simplifies the calculations, is not necessarily fulfilled in the real spin system. A different ratio between the f_i does not violate the strongest hypotheses of the theory. The twinning fraction m_t is also a relevant quantity of the fitting. From the x-ray precession camera photographs we were able to estimate that $m_t \leqslant 0.15$. So we continuously varied this parameter between 0 and 0.15 in order to improve the fitting. The best result was obtained with $m_t = 0.11$. With this constraint, we found $\tilde{D}/k_B = 0.69(4)$ K and $\tilde{E}/\tilde{D} = -0.4(1)$. Deisenhofer *et al.*[10] found also that $\tilde{D}$ and $\tilde{E}$ have opposite sign $(\tilde{E}/\tilde{D} \approx -0.9)$ for $LaMnO_3$ doped with 5% Sr.

The coefficients $\tilde{D}$ and $\tilde{E}$ in Eq. (32) are directly proportional to the magnitude of the distortion modes of the MnO_6 octahedra, $Q_{3g,u} = -1/\sqrt{3}(2l-m-s)$ and $Q_{3g,v} = s-m$. Here we have associated the tetragonal axis with the longest Mn-O distance l along the $\tilde{x}$ direction for the Mn ion at the (0,0,0) site. The $\tilde{y}$ and $\tilde{z}$ axes were taken parallel to the short (s) and medium (m) distances, respectively. The crystal field coefficients are symmetry related[27] and $\tilde{E}/\tilde{D} = -Q_{3g,v}/(\sqrt{3}Q_{3g,u}) = (s-m)/(2l-m-s)$.

Neutron-diffraction data[5] at 200 K gave $-(Q_{3g,v}/Q_{3g,u})/\sqrt{3} = -0.26$. Results for other x values in $La_{1-x}Sr_xMnO_3$ samples ($x = 0.05$, 0.075, and 0.10) indicate that this ratio is only weakly dependent on temperature and Sr concentration, with an average of $-(Q_{3g,v}/Q_{3g,u})/\sqrt{3} = -0.26(6)$. These values imply a ratio $\tilde{E}/\tilde{D}$ that is coincident in sign with our experimental results for the ESR linewidth and close in magnitude. The absolute values of the coefficients are in reasonable agreement.

In order to check the validity of our explanation, we have reproduced the temperature variation of $\alpha(T), \beta(T)$ and $\delta(T)$, assuming that $Q_{3g,u}, Q_{3g,v}$, and consequently $\tilde{D}(T)$ and $\tilde{E}(T)$ are proportional to the orthorhombic distortion of the lattice, $s(T) = \Sigma_{i=1}^3 |a_i - \langle a_i\rangle|/3\langle a_i\rangle$, with $a_i = a$, b, c, and $\langle a_i\rangle$ as defined in Sec. II C. Using the neutron-diffraction data[5,6] we have found that these relations are correct within an uncertainty of about 35%. Thus, the crystal field contributions to $\Delta H_{pp}(\infty)$ result proportional to $s^2(T)$. The empty squares (and the lines connecting them) in Fig. 8 correspond to the normalized curves (to 280 K) calculated using values of $s(T)$ derived from our dilatometry measurements of Fig. 1, and taking the ratio $\tilde{E}(T)/\tilde{D}(T)$ as constant. Since $a,b \geqslant \langle a_i\rangle$ and $c/\sqrt{2} \leqslant \langle a_i\rangle$, $s(T) = [2(\Delta l/l)_{ab} - (\Delta l/l)_c]/3$. The calculated curves follow closely the behavior of α, β, and δ obtained from the ESR experiments.

All the parameters present a step at T_{JT}, followed by a slow decay above the transition. It is interesting to note that the experimental $\beta(T)$ shows, above T_{JT}, a variation even slower than that expected from the thermal expansion. This observation suggests that the local distortions persist up to higher temperatures than the macroscopic ones do.

Below ≈ 250 K, $\Delta H_{pp}(\infty)$ increases rapidly with decreasing temperature as shown in the inset of Fig. 5. Besides crystal field effects, short-range FM ordering could contribute to the broadening of the linewidth in this temperature region. Finite-temperature corrections to the calculations of the previous sections are then needed to explain this broadening. The first correction terms (including only statistical effects) exhibit the same angular dependence of $\Delta H_{pp}(\infty)$ and are proportional to $-J/k_BT$. Therefore, the linewidth will either increase or decrease depending on the sign of the dominant J. In our case the increase observed is compatible with FM interactions [minus sign in Eq. (7b)].

As T_C is approached, the effective g factor, $g_{eff} = h\nu/\mu_B H_R$, deviates anisotropically from its high-temperature value $g_0 = 1.997(3)$ and $\Delta g(\theta,\varphi) \equiv g_{eff}(\theta,\varphi) - g_0 \approx f(\theta,\varphi)(T-T_C)^{-1}$, with $T_C \sim 180$ K.

In order to analyze this behavior we should, first of all, consider the demagnetizing fields which become important in this temperature region. The effects of these fields were also observed in the dc-magnetization measurements, where the shape of the sample provides an extra source of anisotropy. The data taken (under an applied field of 1.5 kgauss) are compatible with the behavior expected for an oblate ellipsoid with a eccentricity of $\varepsilon = 0.5$, which is an adequate approximation for the average dimensions of our sample. Using the corresponding demagnetizing fields (proportional to the measured magnetization) we have calculated the g shifts shown as dashed lines in Fig. 4(b) for $\mathbf{H}//c$ and $\mathbf{H}//[110]$ (ab diagonal). For these orientations most of the experimental g shift is accounted for in this way.

However, when $\mathbf{H}$ is rotated in the ab plane, a significant splitting of the line is observed for $\mathbf{H}$ parallel to the edges of the sample. As already stated in Sec. II B, these orientations correspond to the a (or b) axes of each of the orientation domains. This splitting cannot be interpreted as a demagnetizing effect, and thus we ascribe this observation to ESR lines corresponding to different parts of the crystal with either the a or the b axis pointing along $\mathbf{H}$.

Coming back to Eq. (14) we observe that the g factor is also affected by the finite-temperature corrections. We can express $\Delta g/g$ as

$$\begin{aligned}\Delta g(\theta,\varphi,T)/g = {} & \left[\frac{S(S+1)-3/4}{5k_B(T-T_C)}\right] \\ & \times\left[-\frac{1}{2}(\tilde{D}+3\tilde{E})\left(1-\frac{3}{2}\sin^2\lambda\right)(3\cos^2\theta-1)\right. \\ & \left.+\frac{3}{2}(\tilde{D}-\tilde{E})(\sin 2\eta\cos\lambda)\sin^2\theta\sin 2\varphi\right],\end{aligned} \tag{33}$$

where λ is the tilting angle of the MnO_6 octahedra measured from the c axis and η its rotation in the ab plane. Based on experimental data available from compounds of similar composition,[2,13] we have taken $\lambda = 12°$ and $\eta = 33°$ in our calculations. Note that the DM interaction does not contribute to the g shift, in this order of perturbation. Here, the factor $(k_B T)^{-1}$ may be replaced[28] by $(T-T_C)^{-1}$ since it arises from the mean value of S_z, which is proportional to $\chi(T)$.

In Eq. (33) the measured ratio $\tilde{E}/\tilde{D}$ almost cancel the factor $(\tilde{D}+3\tilde{E})$ and this explains the negligible effect for $\mathbf{H}//c$ or $\mathbf{H}//ab$ diagonal $(\varphi=0)$. Instead, for $\varphi = 45°$ $(\mathbf{H}//a)$ or $\varphi = -45°$ $(\mathbf{H}//b)$, the crystal field contribution to $\Delta g/g$ is maximum, as shown with the continuous lines in Fig. 4(c). In this figure, a temperature dependence for $\tilde{D}(T)$ and $\tilde{E}(T)$ was assumed proportional to the orthorhombic distortion, as discussed previously. Note that the calculated g factors follow qualitatively the experimental behavior. A better quantitative agreement with the experimental data is obtained if the absolute values of both $\tilde{D}$ and $\tilde{E}$ are increased by a factor of about 2 [shown as continuous lines in Fig. 4(c)]. This fact is compatible with out previous calculations since, as there is an arbitrary scaling factor for f_0, f_1, and f_2 in Eqs. (12a) and (12b), this choice would imply only a renormalization of these coefficients. Although for $\mathbf{H}$ away from a (or b), the splitting becomes smaller than the linewidth; numerical simulations of the superimposed spectra allowed us to confirm the $\sin(2\varphi)$ angular dependence in the ab plane.

V. CONCLUDING REMARKS

We have performed a systematic study of the thermal expansion, dc-susceptibility, and ESR spectra of a $La_{7/8}Sr_{1/8}MnO_3$ single crystal in the paramagnetic region across the O'-O-R structural phases. The successful orientation and characterization of the twinning in our sample was crucial to interpret the ESR results. As revealed by the dilatometry measurements, the transition from the O' phase with cooperative Jahn-Teller distortions to the O phase, at $T_{JT} = 282(3)$ K, is very sharp and with very small hysteresis. Above T_{JT}, the local distortions persist and average gradually to zero, giving rise to anomalously large thermal-expansion coefficients. The transition from the O phase to the high-temperature $R\overline{3}c$ phase at $T_R \approx 480$ K was observed in both ESR and susceptibility experiments. We have shown that the Curie-Weiss temperature $\Theta^{CW}(T)$ presents a behavior that reflects the structural changes of the system.

The angular and temperature variations of the g factor and the linewidth were analyzed using a perturbational Kubo-Tomita approach. In our scheme the ideally narrow ESR line is broadened by the crystal field interactions and the DM antisymmetric exchange. With this model, and taking into account the twinning state of the sample, we were able to nicely reproduce the angular variations observed. The temperature dependence of the anisotropy was analyzed in relation to the structural distortions.

ACKNOWLEDGMENTS

We acknowledge partial support from ANPCyT (Argentina) through PICT Grant No. 99 03-05-266, FOMEC (Argentina), and AMORE Project (UE). M.T., M.C.G.P., and G.A. are members of CONICET. The samples studied in this work were synthesized by R.S. at the Laboratoire de Physico-Chimie de L 'Etat Solide, Université Paris Sud, France. We thank the members of the group for their helpful assistance.

APPENDIX A: THE KUBO-TOMITA APPROACH

From Eq. (4) and taking $M_x \cong -\mu_B g S x/V$ with $\widehat{\mathbf{x}\equiv}\ \hat{\mathbf{h}}_1$, it follows from Eq. (8) that

$$[M_{h_1},\mathcal{H}_{exch}] \simeq [\vec{\mathbf{S}},\mathcal{H}_{exch}] = 0. \tag{A1}$$

Recalling that

$$\exp(-i\omega_o S_z t)S_\pm \exp(i\omega_o S_z t) = S_\pm \exp(\mp i\omega_o t),$$

where $\omega_o \equiv g\mu_B H/\hbar$, one can write in the high-temperature approximation

$$\langle M_{h_1}(t,H)M_{h_1}\rangle_{T\to\infty} = \frac{1}{2V^2} g^2\mu_B^2 \sum_{u=\pm 1} \langle \tilde{S}_x(t,H)S_u\rangle_{T\to\infty} \times \exp(-iu\omega_o t)$$

and

$$\tilde{S}_x(t,H) \equiv \exp(-i/\hbar\mathcal{H}_0 t)S_x(t,H)\exp(i/\hbar\mathcal{H}_0 t).$$

The equation of motion for $\tilde{S}_x(t,H)$,

$$\partial_t \tilde{S}_x(t,H) = i/\hbar[\tilde{\mathcal{H}}'(t,H),\tilde{S}_x(t,H)]$$

can be formally solved by successive iterations in terms of increasing orders of $\tilde{\mathcal{H}}'(t,H)$, although this is usually done only up to second order. Given the form of the operators composing $\mathcal{H}'$, it is simple to show that the first-order term vanishes identically because it implies the averaging of an odd number of spin operator components. The second-order contributions have terms[22,29] either independent (secular contributions) or dependent on the frequency ω_o. If only secular terms are retained one gets

$$\begin{aligned}
&\langle \tilde{S}_x(t,H)S_m\rangle_{T\to\infty} \\
&\quad = \langle S_z^2\rangle_{T\to\infty} \sum_{u=\pm 1} \Bigg\{ 1 + i/\hbar \int_0^t \frac{1}{2\langle S_z^2\rangle_{T\to\infty}} \\
&\qquad \times \langle [\tilde{\mathcal{H}}'(\tau),S_{-u}]S_u\rangle_{T\to\infty} d\tau - \frac{1}{2\hbar^2\langle S_z^2\rangle_{T\to\infty}} \\
&\qquad \times \int_0^t (t-\tau)\langle [S_u,\tilde{\mathcal{H}}'(\tau,H)][\mathcal{H}',S_{-u}]\rangle_{T\to\infty} d\tau \Bigg\}.
\end{aligned} \tag{A2}$$

This expression is usually assumed to correspond to the initial terms in the expansion of an exponential function, such that Eq. (4) can be put into the form

$$\begin{aligned}
\chi''(\omega,H)|_{T\to\infty} \simeq {} & \frac{\omega}{4k_BT} g^2\mu_B^2 \left[\frac{\langle S_x^2\rangle_\infty}{\Omega N}\right] \\
& \times \sum_{u=\pm 1} \int_{-\infty}^{\infty} dt\,\Phi_u(t,H) \\
& \times \exp[-i(\omega+u\omega_o)t + i\delta_u(t)],
\end{aligned} \tag{A3}$$

where Ω is the volume of the unit cell ($V=\Omega N$) and

$$\delta_u(t) = \frac{1}{\hbar}\int_0^t \frac{1}{2\langle S_z^2\rangle} \langle [\tilde{\mathcal{H}}'(\tau),S_{-u}]S_u\rangle d\tau, \tag{A4}$$

while the relaxation function Φ_μ is given by

$$\begin{aligned}
\Phi_u(t,H) \simeq \exp\Bigg\{ & -\frac{1}{2\hbar^2\langle S_z^2\rangle_{T\to\infty}} \int_0^t (t-\tau)\langle [S_u,\tilde{\mathcal{H}}'(\tau,H)] \\
& \times [\mathcal{H}',S_{-u}]\rangle_{T\to\infty} d\tau \Bigg\}.
\end{aligned} \tag{A5}$$

After adopting approximately $\rho \simeq (1/\mathrm{Tr}\{\mathbf{1}\})\{\mathbf{1} - (1/\mathrm{kT})\mathcal{H}_{exch} - (\hbar\omega_o/kT)S_z\}$, the first-order terms $\langle [\tilde{\mathcal{H}}'(\tau),S_{-u}]S_u\rangle_{T\to\infty}$ in Eq. (A4) require the calculation of

$$\begin{aligned}
\mathrm{Tr}\{\rho(\tilde{\mathcal{H}}'(\tau)S_xS_+ - \tilde{\mathcal{H}}'(\tau)S_+S_x)\} &= \mathrm{Tr}\{\rho(\tilde{\mathcal{H}}'(\tau)[S_x,S_+])\} \\
&= -2\,\mathrm{Tr}\{\rho\mathcal{H}'S_z\},
\end{aligned}$$

which vanishes as it involve traces taken over an odd number of spin operators, whether $\mathcal{H}'$ refers to $\mathcal{H}_{CF}$ or to $\mathcal{H}_{DM}$. When finite-temperature corrections are included, one may expect contributions that shift the line position from ω_o (see text).

With regard to $\Phi_u(t,H)$, we consider now the case of $\mathcal{H}' \equiv \mathcal{H}_{CF}$. Following standard procedures[21,22,30] for the calculation of the commutators involved, retaining terms independent of ω_o (secular contributions), and keeping only the contributions due to self-correlation functions, we obtained

$$\left.\frac{\langle [S_u,\tilde{\mathcal{H}}'(\tau,H)][\mathcal{H}',S_{-u}]\rangle_\infty}{\langle S_x^2\rangle_\infty}\right|_{\mathrm{sec}} \approx \hbar^2\Delta(\tau)|_{\mathrm{sec}}\,\omega_{CF}^2(0,\theta,\varphi) \tag{A6}$$

with

$$\omega_{CF}^2(0,\theta,\varphi) \equiv \left[\sum_{p=1}^{4}\left(\frac{1}{2\hbar^2}\right)\{3\mathbf{D}_{zz}(p) - \mathrm{Tr}[\mathbf{D}(p)]\}^2\right].$$

Here, the argument 0 implies secular contributions against those nonsecular $\omega_{CF}^2(\pm\omega_o,\theta,\varphi)$ or $\omega_{CF}^2(2\omega_o,\theta,\varphi)$. In Eq. (A6) $\Delta(\tau)|_{\mathrm{sec}}$ can be written as a combination of different spin-correlation functions such as

$$\frac{1}{2\langle S_x^2(0p)\rangle_\infty}\langle [S_z(0p)S_+(0p)]^{exch}_{(\tau)} S_z(0p)S_-(0p)\rangle_\infty,$$

where we have already taken into consideration the periodic properties of the crystal lattice and also that all self-correlation functions should be identical for any of the species (1–4) of the magnetically nonequivalent ions. Then

$$\begin{aligned}
\chi''(\omega,B)|_{T\to\infty} \simeq {} & \frac{\omega}{4k_BT} g^2\mu_B^2 \left[\frac{\langle S_x^2\rangle_\infty}{\Omega N}\right] \\
& \times \int_{-\infty}^{\infty} \{\Phi_{CF}(0,t,\theta,\varphi)\exp[-i(\omega+\omega_o)t] \\
& + \Phi_{CF}(0,t,\theta,\varphi)\exp[-i(\omega-\omega_o)t]\}dt,
\end{aligned} \tag{A7}$$

where

$$\Phi_{CF}(0,t,\theta,\varphi) = \exp\left\{ -\omega_{CF}^2(0,\theta,\varphi)\left(\int_0^{|t|}(|t|-\tau)\Delta(\tau)|_{\sec} d\tau \right) \right\}.$$

If all $\Delta(\tau)$ functions are fast decaying functions of τ, the upper limit of the integral can safely be extended to ∞. Under this assumption, one can see that the first contribution to $\Phi_{CF}(0,t,\theta,\varphi)$ is linear in $|t|$ while the second only produces an irrelevant correction to the amplitude of the signal. Consequently, in the high-temperature limit one arrives to

$$\begin{aligned}\chi''(\omega,B)|_{T\to\infty} &\simeq \frac{\omega}{4k_BT} g^2\mu_B^2 \left[\frac{\langle S_x^2\rangle_\infty}{\Omega N} \right] \\ &\quad \times \exp\left(-\int_0^\infty \tau\Delta(\tau)d\tau \right) \int_{-\infty}^{\infty} \{\exp[-i(\omega+\omega_o)t \\ &\quad -\Gamma_{CF}(\theta,\varphi)|_{\sec}|t|] + \exp([-i(\omega-\omega_o)t \\ &\quad -\Gamma_{CF}(\theta,\varphi)|_{\sec}|t|])\} dt,\end{aligned}$$

which after performing the Fourier's transform will lead to a Lorentzian lineshape. Also

$$\Gamma_{CF}(\theta,\varphi)|_{\sec} \approx \omega_{CF}^2(0,\theta,\varphi)\left(\int_0^\infty \Delta(\tau)|_{\sec} d\tau \right). \tag{A8}$$

Thus, $\Gamma_{CF}(\theta,\varphi)|_{\sec}$ is built from two factors: an angular varying function $\omega_{CF}^2(0,\theta,\varphi)$ which depends on the crystal field tensors at each site projected along the direction of the magnetic field times a term that corresponds to an integral over spin self-correlation functions. If these are taken of Gaussian form, which is usually assumed to be a reasonable approximation for rapidly decaying functions, as expected for the spin correlations in systems forming three-dimensional magnetic networks,[30] one gets

$$\left(\int_0^\infty \Delta(\tau)|_{\sec} d\tau \right) \propto \int_0^\infty \exp\left(-\frac{\omega_{exch}^2\tau^2}{2} \right) d\tau = \frac{1}{\omega_{exch}}\sqrt{\frac{\pi}{2}}.$$

We assumed that ω_{exch} arises from a combination of the exchange parameters $J^2(0\alpha,j\beta)$ as

$$\omega_{exch} = \left[\sum_{p,q;i=0}^{N} \frac{J^2(0p,iq)}{\hbar^2} \right]^{1/2} \approx \sqrt{z\frac{\overline{J^2}}{\hbar^2}}, \tag{A9}$$

with z being the number of first neighbors and $\overline{J^2}$ an average value of the exchange coefficients of Eq. (7b). Therefore, $\Gamma_{CF}(\theta,\varphi)|_{\sec}$ can be written as

$$\Gamma_{CF}(\theta,\varphi)|_{\sec} \propto \frac{\omega_{zf}^2(0,\theta,\varphi)}{\omega_{exch}}$$

showing how the exchange interaction produces narrowing effects on the linewidth. A similar calculation along the same lines can be done to obtain the nonsecular CF contributions to the linewidth. In these cases, as we assume $\omega_{exch} \gg \omega_o$, the following replacement has been used in all of these contributions to the linewidth:

$$\begin{aligned}\int_0^t (t-\tau)\exp\left(-\frac{\omega_{exch}^2}{2}\tau^2 \right)\cos(p\omega_o\tau)d\tau \\ \cong |t|\frac{\sqrt{2}}{\omega_{exch}}\int_0^\infty \exp(-x^2)dx.\end{aligned}$$

Concerned with the DM interaction, one similarly obtains

$$\begin{aligned}&\frac{\mathrm{Tr}([S_-,\tilde{\mathcal{H}}_{DM}(\tau)][\mathcal{H}_{DM},S_+]_\infty)}{\mathrm{Tr}(S_x^2)} \\ &= \mathrm{Tr}[S_z^2(i)]\frac{1}{4}\sum_{j=0}^{N}\sum_{p,q=1}^{k}[\vec{d}(0p,iq)\hat{\mathbf{z}}]^2 \\ &\quad \times \left[\frac{\mathrm{Tr}[(S_z(0p)S_-(jq))_{(\tau)}^{exch}S_z(0p)S_+(jq)]}{\{\mathrm{Tr}[S_z^2(j)]\}^2} \right],\end{aligned}$$

where use has been made of

$$\vec{d}(ip,jq) = -\vec{d}(jq,ip)$$

with

$$\vec{d}(ip,ip) = 0.$$

It is worth remarking that while $\mathcal{H}_{CF}$ is an operator involving only one-site spin operators, $\mathcal{H}_{DM}$ involves two-sites spin operators. Adopting the approximation that four spin-correlation functions involving two different sites can be broken into products of two-spin correlation functions, and retaining only self-correlation terms, one gets (for the secular contribution)

$$\begin{aligned}&\frac{\mathrm{Tr}([S_-,\tilde{\mathcal{H}}_{DM}(\tau)][\mathcal{H}_{DM},S_+]_\infty)}{\mathrm{Tr}(S_x^2)} \\ &\simeq \mathrm{Tr}[S_z^2(i)]\frac{1}{2}\left\{ \frac{\mathrm{Tr}[S_z^{(exch)}(0\alpha,\tau)S_z(0\alpha)]}{\mathrm{Tr}[S_z^2(i)]} \right\}^2 \\ &\quad \times \sum_{p\neq q}\sum_{j=0}^{N}[\vec{d}(0p,jq)\hat{\mathbf{z}}]^2.\end{aligned}$$

These approximations lead to the contribution of the DM interaction to the linewidth given by Eq. (13). Nonsecular contributions of this interaction has been ignored.

APPENDIX B: ADDITIONAL FORMULAS FOR THE CALCULATION OF THE ESR LINEWIDTH

1. Nonsecular terms of the crystal field contribution

a. First-kind terms

$$\begin{aligned}\alpha_{ns(1)}^{CF} = \tfrac{1}{45}[171A^2 + 13B^2 + 10(D^2+E_2^2) + 20E_1^2 - 27F^2 \\ -72G^2 + 20E_1(D+E_2)],\end{aligned}$$

$$\beta^{CF}_{ns(1)}=\tfrac{1}{63}[288A^2-16B^2+14(D^2+E_2^2)+28E_1^2-4.5F^2-9G^2+28E_1(D+E_2)],$$

$$\gamma^{CF}_{ns(1)}=\tfrac{1}{35}[9A^2-0.5(B^2+G^2)+2F^2],$$

$$\delta^{CF}_{ns(1)}=\tfrac{1}{2}[G^2-B^2].$$

b. Second-kind terms

$$\alpha^{CF}_{ns(2)}=\tfrac{1}{30}[54A^2+8B^2+50(D^2+E_2^2)-50E_1^2+168F^2+288G^2+40E_1(D+E_2)-60DE_2],$$

$$\beta^{CF}_{ns(2)}=\tfrac{1}{21}[54A^2-4B^2+14(D^2+E_2^2)-56E_1^2-12F^2+24G^2-56E_1(D+E_2)-84DE_2],$$

$$\gamma^{CF}_{ns(2)}=\tfrac{1}{35}[9A^2+0.5(B^2+G^2)-2F^2],$$

$$\delta^{CF}_{ns(2)}=\tfrac{1}{2}[B^2-G^2].$$

2. Crystal field tensors expressed in the local and laboratory coordinate frames

In the local coordinate frame $(\tilde{x},\tilde{y},\tilde{z})$, we have proposed the following CF Hamiltonian:

$$\mathcal{H}^{CF}_{local}=\tilde{D}S^2_{\tilde{x}}+\tilde{E}(S^2_{\tilde{y}}-S^2_{\tilde{z}}).$$

Parametrizing the rotations of the local system with respect to the crystallographic frame (ξ,η,ς) by the two Euler angles λ and η (tilting from ς axis and rotation in the $\xi\eta$ plane, respectively), we found

$$D=-\tfrac{1}{2}(\tilde{D}+\tilde{E})(\cos^2\eta\cos^2\lambda+\sin^2\eta)-\tfrac{1}{2}(\tilde{D}-\tilde{E})\cos\lambda\,\sin2\eta+\tilde{E}\cos^2\eta\sin^2\lambda,$$

$$E_1=\tfrac{1}{2}(\tilde{D}+\tilde{E})\sin^2\lambda-\tilde{E}\cos^2\lambda,$$

$$E_2=-\tfrac{1}{2}(\tilde{D}+\tilde{E})(\sin^2\eta\,\cos^2\lambda+\cos^2\eta)+\tfrac{1}{2}(\tilde{D}-\tilde{E})\cos\lambda\,\sin2\eta+\tilde{E}\sin^2\eta\,\sin^2\lambda,$$

$$F_1=-\tfrac{1}{2}(3\tilde{E}+\tilde{D})\cos\eta\,\sin2\lambda-(\tilde{D}-\tilde{E})\sin\lambda\,\sin\eta,$$

$$F_2=\tfrac{1}{2}(\tilde{D}+3\tilde{E})\sin\eta\,\sin2\lambda-(\tilde{D}-\tilde{E})\sin\lambda\,\cos\eta,$$

$$G=\tfrac{1}{2}(\tilde{D}+\tilde{E})\sin2\eta\,\sin^2\lambda+(\tilde{D}-\tilde{E})\cos\lambda\,\cos2\eta+\tilde{E}\sin^2\lambda\,\sin2\eta.$$

---

[1] M.T. Causa, G. Alejandro, R. Zysler, F. Prado, A. Caneiro, and M. Tovar, J. Magn. Magn. Mater. **196-197**, 506 (1999).

[2] J. Rodríguez-Carvajal, M. Hennion, F. Moussa, A.H. Moudden, L. Pinsard, and A. Revcolevschi, Phys. Rev. B **57**, R3189 (1998).

[3] D. Louca, T. Egami, E.L. Brosha, H. Röder, and A.R. Bishop, Phys. Rev. B **56**, 8475 (1997).

[4] V.A. Ivanshin, J. Deisenhofer, H.A. Krug von Nidda, A. Loidl, A.A. Mukhin, A.M. Balbashov, and M.V. Eremin, Phys. Rev. B **61**, 6213 (1999).

[5] Tapan Chatterji, Bachir Ouladdiaf, P. Mandal, B. Bandyopadhyay, and B. Ghosh, Phys. Rev. B **66**, 054403 (2002).

[6] L. Pinsard, J. Rodríguez Carvajal, and A. Revcolevschi, J. Alloys J. Alloys Compd. **262-263**, 152 (1997); L. Pinsard, J. Rodríguez Carvajal, A.H. Moudden, A. Anane, A. Revcolevschi, and C. Dupas, Physica B **234-236**, 856 (1997).

[7] M. Tovar, G. Alejandro, A. Butera, A. Caneiro, M.T. Causa, F. Prado, and R.D. Sánchez, Phys. Rev. B **60**, 10199 (1999).

[8] G. Alejandro, M.T. Causa, C.A. Ramos, M. Tovar, and J. Fontcuberta, J. Magn. Magn. Mater. **226-230**, 2002 (2001).

[9] G. Alejandro, C.A. Ramos, D. Vega, M.T. Causa, J. Fontcuberta, and M. Tovar, Physica B **320**, 26 (2002).

[10] J. Deisenhofer, M.V. Eremin, D.V. Zakharov, V.A. Ivanshin, R.M. Eremina, H.A. Krug von Nidda, A.A. Mukhin, A.M. Balbashov, and A. Loidl, Phys. Rev. B **65**, 104440 (2002).

[11] A. Revcolevschi and R. Collongues, C. R. Seances Acad. Sci., Ser. C **266**, 1767 (1968); A. Revcolevschi, Rev. Int. Hautes Temp. Refract. **7**, 73 (1970).

[12] H.R. Salva, C.A. Ramos, A.A. Ghilarducci, R.D. Sánchez, and C. Vázquez-Vázquez, J. Magn. Magn. Mater. **226-230**, 590 (2001).

[13] B. Dabrowski, X. Xiong, Z. Bukowski, R. Dybzinski, P.W. Klamut, J.E. Siewenie, O. Chmaissem, J. Shaffer, C.W. Kimball, J.D. Jorgensen, and S. Short, Phys. Rev. B **60**, 7006 (1999).

[14] J. Rodríguez Carvajal (private communication).

[15] M.T. Causa, M. Tovar, A. Caneiro, F. Prado, G. Ibáñez, C.A. Ramos, A. Butera, B. Alascio, X. Obradors, S. Piñol, F. Rivadulla, C. Vázquez-Vázquez, A. López-Quintela, J. Rivas, Y. Tokura, and S.B. Oseroff, Phys. Rev. B **58**, 3233 (1998).

[16] D.L. Huber, G. Alejandro, A. Caneiro, M.T. Causa, F. Prado, M. Tovar, and S.B. Oseroff, Phys. Rev. B **60**, 12 155 (1999).

[17] H. Nojiri, K. Kaneko, M. Motokawa, K. Hirota, Y. Endoh, and K. Takahashi, Phys. Rev. B **60**, 4142 (1999).

[18] J. Nogués, V. Skumryev, J.S. Muñoz, B. Martínez, J. Fontcuberta, L. Pinsard, and A. Revcolevschi, Phys. Rev. B **64**, 024434 (2001).

[19] H. Aliaga, M.T. Causa, M. Tovar, A. Butera, D. Vega, B. Alascio, G. Leyva, G. Polla, and P. König, B. Alascio, J. Phys.: Condens. Matter. **15**, 249 (2003).

[20] M. Tovar, M.T. Causa, A. Butera, J. Navarro, B. Martínez, J. Fontcuberta, and M.C.G. Passeggi, Phys. Rev. B **66**, 024409 (2002).

[21] R. Kubo and K. Tomita, J. Phys. Soc. Jpn. **9**, 888 (1954).

[22] G.E. Pake, *Paramagnetic Resonance*: *An Introductory Monograph* (Benjamin, New York, 1962).

[23] A. Abragam, *The Principles of Nuclear Magnetism* (Oxford University Press, London, 1961).

[24] S. Dattagupta, *Relaxation Phenomena in Condensed Matter Physics* (Academic Press, New York, 1987).

[25] M.C.G. Passeggi and R. Calvo, J. Magn. Reson. Ser. A **114**, 1 (1995).

[26] I. Solovyev, N. Hamada, and K. Terakura, Phys. Rev. Lett. **76**, 4825 (1996).

[27] R. Calvo, Ph.D. thesis, Instituto Balseiro, Universidad Nacional de Cuyo, Argentina, 1969.

[28] N.O. Moreno, P.G. Pagliuso, C. Rettori, J.S. Gardner, J.L. Sarrao, J.D. Thompson, D.L. Huber, J.F. Mitchell, J.J. Martinez, and S.B. Oseroff, Phys. Rev. B **63**, 174413 (2001).

[29] On several stages in the process of calculation one is confronted with expressions such as $\exp(-im\omega_o S_z \tau) S_{\pm} \exp(im\omega_o S_z \tau) = \exp(\mp im\omega_o \tau) S_{\pm}$, where m is an integer resulting from the addition or subtraction among other integers. Those leading to $m \neq 0$ generate the nonsecular terms and involve exponential factors such as $\exp(\mp im\omega_o \tau)$, which give rise to both real and imaginary contributions. When these are modulated by rapidly decaying functions as compared with their oscillation periods (as it is assumed in this paper), they are replaced by $\simeq 1$.

[30] P.M. Richards, in *Local Properties at Phase Transitions*, edited by K.A. Mueller and A. Rigamonti (North-Holland, New York, 1976), p. 539.